

New approach to measurement of the three dimensional crystallization front propagation velocity in strongly coupled complex plasma

D. I. Zhukhovitskii

*Joint Institute of High Temperatures, Russian Academy of Sciences,
Izhorskaya 13, Bd. 2, 125412 Moscow, Russia and*

Moscow Institute of Physics and Technology, Institutsky lane 9, Dolgoprudny, Moscow region, 141700 Russia

V. N. Naumkin,* V. I. Molotkov, and A. M. Lipaev

Joint Institute of High Temperatures, Russian Academy of Sciences, Izhorskaya 13, Bd. 2, 125412 Moscow, Russia

H. M. Thomas

*Institut für Materialphysik im Weltraum, Deutsches Zentrum für Luft
und Raumfahrt (DLR), Münchener Str. 20, 82234 Wessling, Germany*

(Dated: July 1, 2019)

The PK-3 Plus laboratory onboard the International Space Station is used to form complex plasma with a liquidlike particle subsystem in metastable state and to observe the propagation of crystallization fronts corresponding to the surfaces of crystal domains. We propose the “axis” algorithm of solidlike particles identification, which makes it possible to isolate different domains and their surfaces as well. Determination of the three-dimensional front velocity is based on its definition implying that there exists a small area of the domain surface propagating along some line perpendicularly to it. The velocity measured in this way is an important characteristic of the plasma crystallization kinetics. It proves to be almost independent of time and the direction of front propagation and amounts to ca. $60\text{--}80\ \mu\text{m s}^{-1}$.

PACS numbers: 52.27.Lw, 64.70.D, 87.15.nt

I. INTRODUCTION

A low-temperature plasma that contains dust particles typically in the range from tens of nanometer to thousands of micrometers is commonly called complex (or dusty) plasma [1–6]. Dusty plasmas are present in astrophysical objects such as comets, protoplanetary discs, or planetary rings [7]. Complex plasmas are specially prepared to study fundamental processes in the strong coupling regime on the most fundamental (kinetic) level, through the observation of individual microparticles and their interactions. In ground-based experiments, the microparticles are heavily affected by the force of gravity. Under microgravity conditions, e.g. on the International Space Station (ISS), gravity is compensated by the ISS orbital motion [8–15]. Due to the high mobility of electrons, particles acquire a significant (macroscopic) negative electric charge. As a result, the particles are pushed out of the strong electric field region close to the electrodes. Thus, they can form expanded almost homogenous particle clouds in the bulk of the low-pressure gas discharge. Also, due to the large particle charge, such subsystem can form a three-dimensional (3D) complex plasma analog of a condensed state that has an ordered structure. We will term the particle subsystems “liquidlike” and “solidlike” (dust crystal) if the dust cloud is similar to a liquid or a solid, respectively.

The dust crystal can undergo phase transitions similar to that in an equilibrium system, in particular, the melting–crystallization first-order transition [1, 15].

Strongly coupled electron-ion plasmas are encountered in numerous physical and astrophysical situations, e.g., inertially confined laboratory plasmas, liquid metals, stellar and planetary interiors, and supernova explosions [16]. Under certain conditions, one can expect the plasma crystallization process associated with the front propagation.

The most valuable information can be gained from observations of the phase transition kinetics. In ground-based experiment [17], growth of a crystal domain in the “liquidlike” dust cloud was observed. Based on the crystallization front visualization, the authors observed its propagation. However, an insufficient system homogeneity and the absence of 3D scanning did not make it possible to measure the “true” 3D front velocity. Instead, only one velocity component in the plane of the system light illumination was estimated on the order of magnitude. Note that the growth of solid phase nuclei in “supercooled” colloidal systems [18, 19] is similar to the processes occurring in complex plasma.

We used the PK-3 Plus laboratory onboard the ISS [12, 20, 21] to form a “supercooled” liquidlike microparticles system and to observe formation and growth of the crystal domains containing $\gtrsim 10^4$ particles each. Due to depth scans performed during the experiment, we can recover 3D coordinates of each microparticle. Then we use and compare different methods to isolate individual crystal domains and their surfaces.

* naumkin@ihed.ras.ru

The objective of this work is to measure the 3D crystallization front velocity. This task is complicated by two facts. First, the domain surface is quite irregular, and the intervals between successive depth scans are too long so that the displacement between corresponding points of the propagating front cannot be determined directly. Second, the finite scan velocity results in surface distortion, which means that the visible and true domain surfaces are different. We solve these problems by determination of a small flat area of the domain surface that propagates along some line and is normal to this line (direction of the rectilinear propagation). This enables one to measure the displacement of this area between successive scans and thus to determine the front velocity.

The paper is organized as follows. In Sec. II, the experimental setup and procedure are discussed in detail. In Sec. III, we use and compare different methods for identification of the “solidlike” particles that comprise the crystal domains and isolate the domain surface. In Sec. IV, the rectilinear propagation definition of the crystallization front velocity is proposed. The data on the front velocity measurement are discussed in Sec. V. The results of this study are summarized in Sec. VI.

II. EXPERIMENTAL SETUP AND PROCEDURE

In the PK-3 Plus laboratory the plasma is excited by an rf-generator of 4W maximum at 13.56MHz with a symmetrical output to drive both electrodes in a push-pull mode. This symmetrical coupling provides a symmetric distribution of the plasma between the two electrodes. A schematic of the experiment is shown in Fig. 1. Details on the setup can be found in [12]. The electrodes are aluminum disks with a diameter of 6 cm and are 3 cm apart.

The optical particle detection system consists of a laser diode with optics that shapes a “laser sheet” perpendicular to the electrode surface and the video cameras. The progressive scan CCD-cameras observe the scattered light at 90° with different magnifications and fields of view. The quadrant camera shows the left part of the interelectrode system (about half of the full system) with a field of view (FOV) of $35.7 \times 26.0 \text{ mm}^2$. The highest magnification camera can be moved along the central vertical axis and has a FOV of $8.1 \times 5.9 \text{ mm}^2$ and is used for high-precision measurement of the microparticles position. The fields of view of the two cameras are shown in Fig. 1. The cameras follow the PAL standard, have a resolution of 768×576 pixels, and provide the two composite 25 Hz interlaced video channels each. We have mixed these two channels to a 50 Hz progressive scan video. The cameras and lasers are mounted on a horizontal translation stage allowing a depth scan through and, therefore, a 3D view of the complex plasma [15, 22, 23].

For manipulation and excitation of the complex plasma, a low-frequency function generator was utilized.

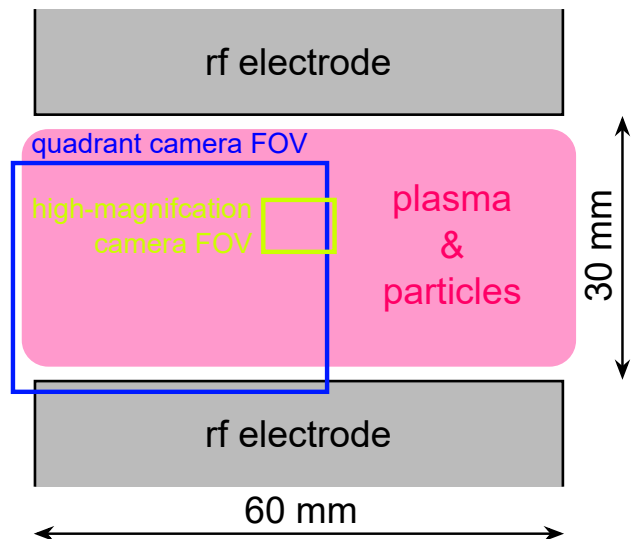


FIG. 1. Sketch of the PK-3 Plus plasma chamber[12]. Fields of view (FOV) of different videocameras are shown.

The function generator provides amplitudes at low frequencies to the electrodes, overlaid on the rf signal. Frequencies between 1 and 255 Hz with amplitudes up to $\pm 55 \text{ V}$ can be set with different waveforms and even different phases between the electrodes [12].

The experiment proceeded as follows. After formation of the plasma in argon, $1.55 \mu\text{m}$ diameter silica particles were injected into it, and the pressure was reduced to 10 or 15 Pa. The pressure was maintained constant in the course of the experiment. The measured effective rf-electrode voltage was equal to 14.9 V and 14.4 V for 10 and 15 Pa, respectively. Under these conditions, due to the intense flux of ions streaming from the discharge center, a space free from micro particles (void) is formed in the vicinity of the cloud center. In spite of the void, almost uniform microparticle number density $n_d = 7.4 \times 10^5 \text{ cm}^{-3}$ in the high-magnification camera FOV is established. Then, the function generator was turned on at the frequency 255 Hz (that is above the dusty plasma frequency which according to the estimation for the experimental conditions is less than 100 Hz) and the voltage of 13 V for 10 s. The result of low frequency excitation is a drastic change of the plasma parameters. The evidence of this is the void behavior which is nearly disappeared (like in [12]) and the dust cloud turned into a highly homogeneous system in the high-magnification camera FOV. Next, the function generator was turned off for 5 s and then it was turned on again at the voltage of 20 V. Note that this value of the voltage is less than the threshold voltage at which string formation takes place. In addition, the threshold voltage is greater for smaller particle sizes [24], i.e. the conditions of our experiments are far from those of the string formation. As a result of such manipulation, the initial dust crystal was brought into a liquidlike state in FOV of the high-magnification camera. Thus, the function generator

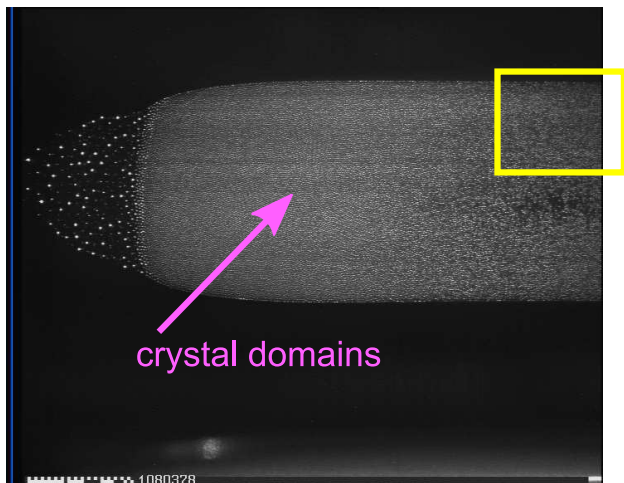


FIG. 2. Side view of dust cloud obtained by the quadrant camera a short time after the function generator pulse. The yellow rectangle shows the high-magnification camera FOV. The purple arrow points to the region where the crystal domains have survived.

was used here for preparation of a “supercooled” system, since the kinetic energy pumped into the microparticles dissipates in less than a second due to the Epstein neutral gas drag. Note that some minor crystal domains survive “shaking” by the function generator. However, these domains lie outside the view of the high-magnification camera, and one can see some domains by the “quadrant” camera (Fig. 2) that has a wider FOV. Then these peripheral crystal domains start to grow in all directions and, eventually, they appear in FOV of the high-magnification camera. The domain growth was observed with and without depth scans by the high-magnification camera. Nine forth and nine back depth scans were performed. The depth and the velocity u of each scan were 4.8 mm and 0.6 mm s^{-1} , respectively. Thus, one scan takes 8 s. The observation time between two successive scans was 3.7 s. Thus, the scans period was 23.4 s. Note that we also performed the crystallization without the low frequency excitation. We observed that the front propagation was too fast and the system in FOV was crystallized within a single scan period, which prevented the observation of the front propagation.

The video images recorded by the high-magnification camera allowed one to observe appearance and growth of the crystallization domains within FOV of this camera. The motion of the domain boundary illuminated by the laser sheet was observed in experiments without scans. With this purpose, the sequences of 100 video frames were superimposed in separate images with the interval of 10 frames, i.e., the resulting images are combinations of the initial frames from 1 to 100, from 10 to 110, etc. In these images, the particles forming a crystal remain confined in their cells while the liquid particles move at about the interparticle distance. Thus, the particles belonging to the crystal form bright spots while the traces

of particles from liquid are blurred over the frame, which makes the crystallization front visible (Fig. 3). Although this figure is a good illustration of the crystallization process, a two-dimensional (2D) video is insufficient for the determination of the 3D crystallization front propagation velocity, in particular, due to the fact that the velocity vector can lie outside the observation plane. For this purpose, we recovered the front surfaces at different instances from the depth scan data.

III. IDENTIFICATION OF THE CRYSTALLIZATION FRONT

The high-magnification camera FOV and scan depth restrict the volume accessible for investigation. It contains over 150000 particles. We employed the method of 3D particle coordinate determination [21]. In what follows, we use the coordinate system with the Z -axis being the symmetry axis directed from the discharge center to an electrode. The X -axis lies in the plane of the laser sheet while the Y -axis is perpendicular to this plane. The direction of the latter coincides with the direction of odd scans. The coordinate system origin finds itself in the center of the discharge. One can conclude from the video illustrated by Fig. 3 that the first domain emerges in the volume of observation at the seventh scan and then the volume occupied by the crystal phase increases until the 11-th scan, where all domains cease to grow. Further, the whole volume is filled with adjoined crystal domains (but the near-sheath region, where crystallization is impossible). Hence, it is sufficient to treat the data from scan #7 to 11.

The first task is the identification of “solidlike” and “liquidlike” particles followed by isolation of individual domains. The widely used method, the correlation criterion is based on the introduction of the local order parameter [25, 26]

$$\bar{q}_{lm}(i) = \frac{1}{N_i} \sum_{j=1}^{N_i} Y_{lm}(\hat{\mathbf{r}}_{ij}), \quad (1)$$

where Y_{lm} are the spherical harmonics[27], $\hat{\mathbf{r}}_{ij} = (\mathbf{r}_j - \mathbf{r}_i)/|\mathbf{r}_j - \mathbf{r}_i|$ is the unit vector that specifies the direction from the particle i to its neighbor j , \mathbf{r}_i and \mathbf{r}_j are the radius-vectors of the respective particles, and the sum runs over all N_i nearest neighbors of the particle i . Here and in what follows, we use the SANN algorithm [28] for the definition of the nearest neighbors.

The local order parameter (1) makes it possible to define the correlation coefficient for a pair of particle i and j

$$\kappa_{ij} = \frac{\sum_{m=-6}^6 \bar{q}_{6m}(i) \bar{q}_{6m}(j)^*}{\left[\sum_{m=-6}^6 |\bar{q}_{6m}(i)|^2 \sum_{m=-6}^6 |\bar{q}_{6m}(j)|^2 \right]^{1/2}}, \quad (2)$$

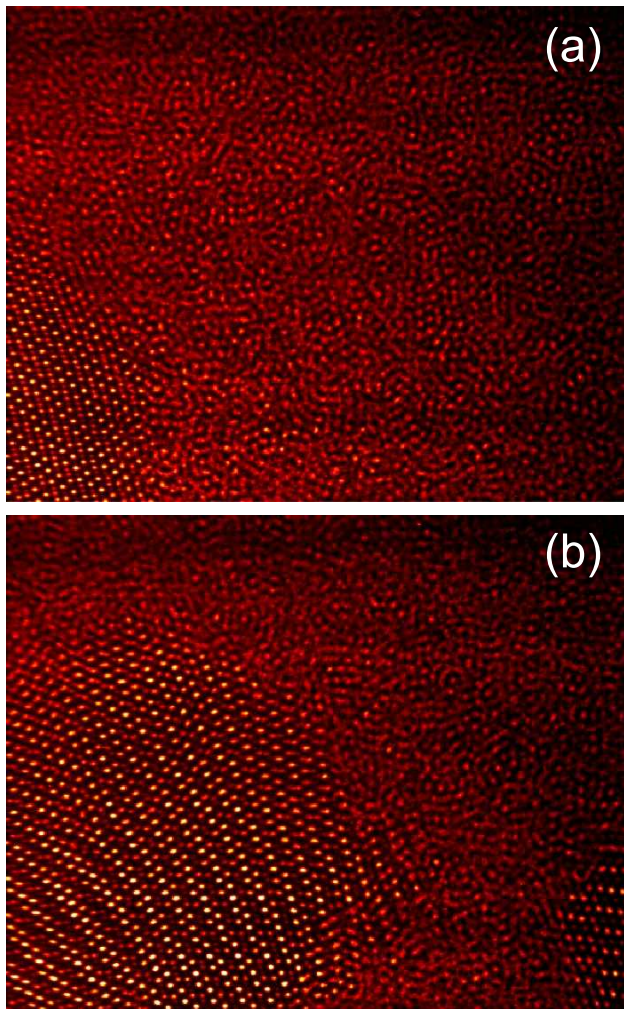


FIG. 3. Demonstration of the liquidlike metastable dust cloud crystallization. Each image is a superposition of 100 consecutive frames (see text); phases (a) and (b) are separated by ca. 20 s.

where asterisk denotes complex conjugation. According to [26] we identify the particle i as a “solidlike” one if it has at least 11 nearest neighbors, for which $|\kappa_{ij}| > 0.5$ (in this case, we call the particles i and j highly correlated). Such correlation criterion proved to be a powerful tool in separation of individual particles into the group of “solidlike” and “liquidlike” ones. Thus, one can effectively define the interface between the phases. However, this criterion is incapable of identification of the interface between different crystal domains and hence, it cannot isolate them. Instead, the objective of this study is investigation of the interface including its parts contacting with other domains. Thus, it is very important for our problem to develop an alternative algorithm that is capable of identifying both particles and domains.

The idea of the algorithm we used is based on the fact that the orientation of the crystal axes is different for different domains. Thus, one can distinguish whether a particular particle belongs to a given domain if the direc-

tions to its nearest neighbors are close to the directions of the crystal axes. Bearing this in mind, for each particle, we try to find pairs of almost opposite nearest neighbors, which define the orientation of the unit cell. Then we do the same for one of the neighboring particles and check whether the next unit cell has the same orientation. Due to slight distortions, the directions of all pairs may not coincide, so we restrict the number of coincidences to five. If this is the case, we identify both particles as solidlike ones pertaining to the same domain.

We will term this the “axis” algorithm. It is realized in the following way. We choose the k -th particle with the radius-vector \mathbf{R}_k at random and find all N_k nearest neighbors. At this step, we consider the k -th particle as a “central” one belonging to the treated domain. Let $\mathbf{R}_l = \mathbf{r}_i^{(k)}$ be the radius-vector of one of its nearest neighbors, where l is the numeration of this particle in the whole system. As a local characteristic of the crystalline lattice, we introduce the matrix $\rho_{ij}^{(k)} = |\mathbf{r}_i^{(k)} + \mathbf{r}_j^{(k)} - 2\mathbf{R}_k|$. We will term counterparts the two nearest neighbors defined by the indexes i_0 and j_0 if for fixed $i = i_0$, $\rho_{i_0 j}$ is minimized at $j = j_0$ as j runs from 1 to N_k and, reciprocally, for fixed $j = j_0$, ρ_{ij_0} is minimized at $i = i_0$ as i runs from 1 to N_k . If an additional condition $\rho_{ij}^{(k)} < \rho_c$, where ρ_c is some small distance parameter, is satisfied then we define the unit vector $\mathbf{d}_{ij}^{(k)} = (\mathbf{r}_i^{(k)} - \mathbf{r}_j^{(k)}) |\mathbf{r}_i^{(k)} - \mathbf{r}_j^{(k)}|^{-1}$. For the counterparts in an ideal lattice, $\rho_{ij}^{(k)} = 0$, and $\mathbf{d}_{ij}^{(k)}$ defines the direction of a crystal axis. Thus, we form a set of the vectors $\mathbf{d}_{ij}^{(k)}$ corresponding to all found pairs of the counterparts. Then, this procedure is repeated for the nearest neighbor with the radius-vector \mathbf{R}_l , and a set of the vectors $\mathbf{d}_{ij}^{(l)}$ is generated. If at least $\eta = 5$ pairs of the vectors $\mathbf{d}_{ij}^{(k)}$ and $\mathbf{d}_{ij}^{(l)}$ satisfy the condition

$$|\mathbf{d}_{ij}^{(k)} \cdot \mathbf{d}_{ij}^{(l)}| > 1 - \varepsilon, \quad (3)$$

where $\varepsilon > 0$ is a parameter, then by definition, this neighbor belongs to the same domain. Otherwise, this neighbor is ignored in what follows. In so doing, we compare the local directions of the crystal lattice vectors (or antiparallel ones), which were determined most reliably.

For an ideal lattice, the corresponding pairs would satisfy the relation $|\mathbf{d}_{ij}^{(k)} \cdot \mathbf{d}_{ij}^{(l)}| = 1$. For our system, the optimum parameters that provide the sharpest domain identification proved to be $\rho_c = 50 \mu\text{m}$ and $\varepsilon = 9.73 \times 10^{-3}$. The parameter ρ_c is still much less than the doubled mean interparticle distance $|\mathbf{r}_i^{(k)} - \mathbf{r}_j^{(k)}| \sim 2n_d^{-1/3} = 221 \mu\text{m}$, and the choice of ε ensures that the least angle between the vectors $\mathbf{d}_{ij}^{(k)}$ and $\mathbf{d}_{ij}^{(l)}$ or between $\mathbf{d}_{ij}^{(k)}$ and $-\mathbf{d}_{ij}^{(l)}$ is less than 8° . Obviously, these parameters can be sensitive to the lattice parameters.

At the next step, we choose the next nearest neighbor until all of them are checked. Likewise, the particles that

satisfy condition (3) are marked as the ones belonging to the treated domain. Otherwise, they are marked as non-domain particles. However, they are still taken into account as the nearest neighbors for a “central” particle other than the k -th particle and, in principle, they can be added to the domain provided that the condition (3) is satisfied for them. Then, we consider one of the neighbor particles as a “central” one and repeat the entire procedure, etc., until all the particles that form the domain are detected. At the next stage, we select randomly the next initial particle not belonging to any domain and find a new domain until all of them are detected.

A comparison between this “axis” algorithm and the correlation criterion shows that both methods mark almost the same particles as “solidlike” ones if η is properly adjusted ($\eta < 5$). However in this case, the “axis” algorithm is incapable of separation of different domains as well as the correlation criterion. The above-selected parameter $\eta = 5$ is the minimum one that solves the problem of separation. Albeit the number of “solidlike” particles in this case is more than 25% lower than that resolved by the correlation criterion (for scan #7), the mismatch takes place mainly near the domain surface and the planes that confine the camera FOV and scan depth (see Fig. 4). In addition, all particles defined as “solidlike” by the “axis” algorithm are either labeled likewise by the correlation criterion or they are highly correlated. Note that the shape of the solid-liquid interface that depends weakly on the particle number proves to be little different for both methods. Figure 4 shows individual crystal domains for scan #11 resolved on the basis of the “axis” algorithm, for which the number of the “solidlike” particles is maximum. The differently oriented crystal lattices are clearly seen in this figure.

It is of interest to determine the type of the crystalline structure for the treated domains. For this purpose, we can apply the axis method described above. Due to the approximate periodicity of a real lattice, the points in space defined by the vectors $\mathbf{r}_l^{(k)} - \mathbf{R}_k$ that define the coordinates of the l th particle relative to the coordinate system with the origin at the location of the k th particle (l and k enumerate the particles in a whole domain) form clusters. We determine the centers-of-mass $\bar{\mathbf{R}}_m$, where m enumerates clusters, for such clusters using the K -means algorithm [29]. The points $\mathbf{0}$ and $\bar{\mathbf{R}}_m$ form a virtual “averaged” lattice, which, by and large, does not coincide with a real one due to the lattice defects, thermal motion of the particles, and the peculiarities of a crystalline symmetry (e.g., for the hcp type lattice, such virtual lattice is quite different from hcp). Then we perform the Voronoi tessellation of this virtual lattice and isolate a single Voronoi cell around the point $\mathbf{0}$. Thus, we obtain a polyhedron that can be indexed by the number and type of its faces (Fig. 5).

We applied this algorithm, which will be discussed in detail elsewhere, to the simulated “noisy” bcc, fcc, and hcp lattices deformed by random shifts of the particles from their equilibrium positions in a crystalline lattice.

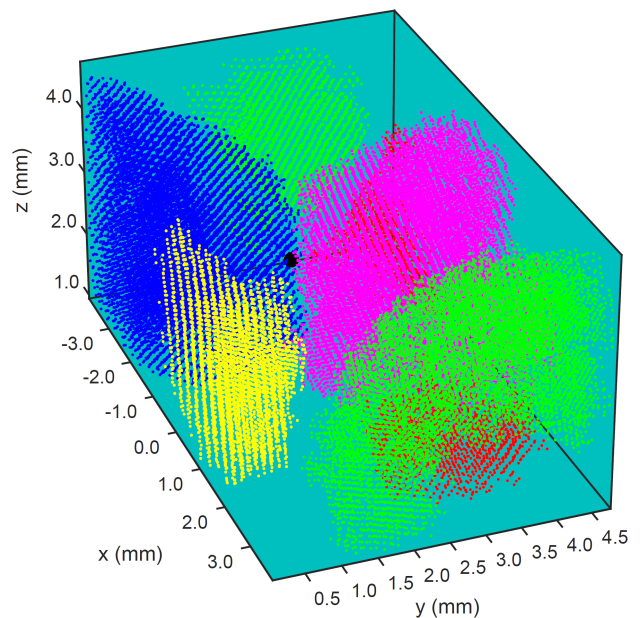


FIG. 4. Domains of the true “crystallike” particles for scan #11 resolved on the basis of the “axis” algorithm. Color indicates particular orientation of the crystal axes. The “liquidlike” particles and the crystal domains containing less than 1000 particles are not shown. Black circle at the interface of the blue-colored domain indicates the intersection with the line along which the crystallization front propagation is treated (the line of rectilinear propagation).

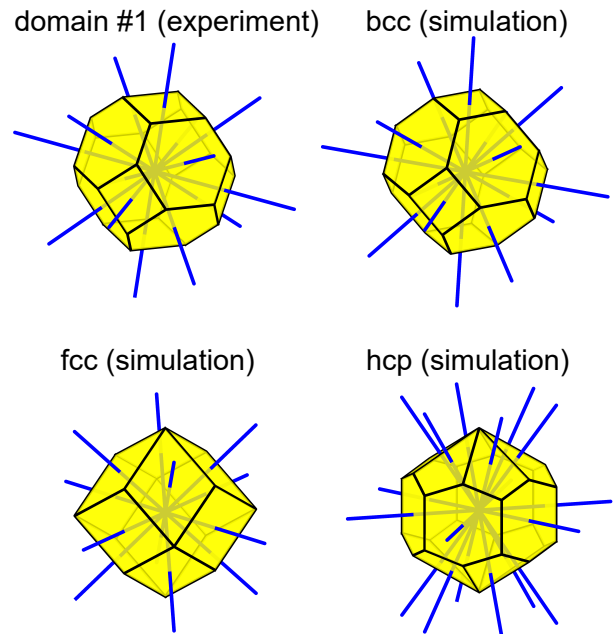


FIG. 5. Voronoi cells calculated from the virtual lattices for the experimental domain (the blue-colored domain in Fig. 4) and the simulated bcc, fcc, and hcp crystalline lattices.

We found that corresponding polyhedrons are fully independent of the shift amplitude provided that it is not too large and that they can be indexed as follows. The bcc polyhedron has six quadrangular and eight hexagonal faces; the fcc polyhedron, 12 quadrangular faces; and the hcp polyhedron, 12 quadrangular and six hexagonal faces. Comparison between the indexes for the blue-colored domain in Fig. 4 (domain #1) and the simulated bcc reveals an exact match and a total mismatch with the simulated fcc and hcp, whence it follows that the lattice type is bcc. The magenta-colored domain in Fig. 4 (domain #2), to which the above-discussed procedure was applied, appeared to be of the same bcc type. Note that no evidence of the crystalline anisotropy follows from Fig. 5: the polyhedron seems almost symmetric. The absence of anisotropy under compatible experimental conditions was noted in [30]. Note that all analyzed experimental domains (consisting of more than 100 particles) have the bcc structure. This is true for the experiment with the gas pressure of 15 Pa (domains #3 and 4, see Sec. IV). In particular, the bcc structure has been observed in the dusty plasma studied at the ground-based facility [31] analogous to the PK-3 Plus facility.

For the further analysis, we select the domain #1 as it is the largest one. At this stage, our objective is the definition of the crystallization front. If we neglect the fluctuations of the domain boundary on the interparticle distance scale and assume the rectilinear propagation of a front small area (see Sec. IV) then some arbitrariness is involved in the front definition. In this case, the distance between this front and the equimolar surface has no physical meaning, similar to the definition of the surface of tension for a plane interface. For example, it is not important whether highly correlated particles that have less than 11 highly correlated neighbors (mostly, the boundary particles) are included in the front definition. One only needs to use the same front definition for all treated scans. Hence, it is sufficient to isolate a monolayer of the particles at the surface of a domain that comprises only true “solidlike” particles. This monolayer consists of pivot particles for the crystallization front. Isolation of the surface monolayer is performed using the algorithm [32] that proved good at the Lennard-Jones cluster surface determination. According to it, the particle 1 with the radius-vector \mathbf{r}_1 that belongs to the domain will be called internal if there exists at least a single particle 2 with the radius-vector \mathbf{r}_2 belonging to the same domain that has more than four nearest neighbors such that the conditions

$$\mathbf{r}_1 \cdot \mathbf{r}_2 > r_1^2, \quad r_2^2 - \frac{(\mathbf{r}_1 \cdot \mathbf{r}_2)^2}{r_1^2} < L^2, \quad (4)$$

are satisfied. Here, L is the length parameter on the order of the interparticle distance. The particles that are not internal and have more than four nearest neighbors are the surface (or pivot) particles.

For this definition, we shift the origin of the coordinate system to the point ($x = -4$ mm, $y = 0$, and

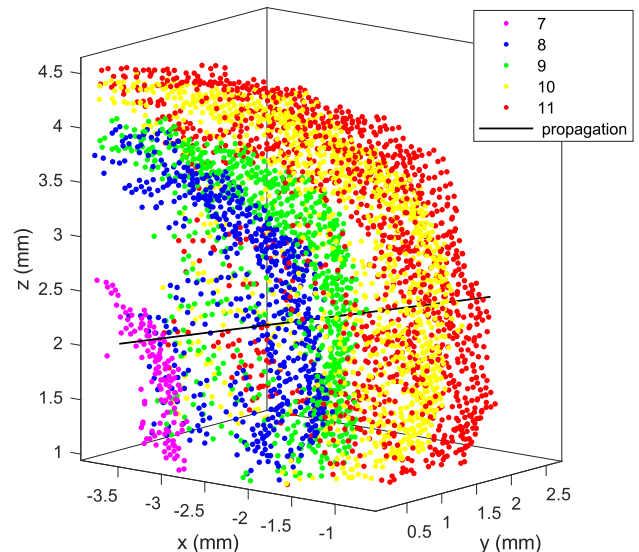


FIG. 6. Development of the crystallization front in time for the blue-colored domain in Fig. 4. Shown are the domain surfaces determined using (4) corresponding to scans #7–11. The scan numbers are color-coded (see legend). Solid line indicates the front propagation direction.

$z = 0.9$ mm). The l.h.s. of the second condition (4) is the squared distance between particle 2 and the axis passing through the coordinate system origin and the particle 1. We set $L^2 = 0.45r_{\min}^2$, where r_{\min} is the distance between the particle 1 and its closest neighbor. The results of the definition of crystallization front for scans #7–11 are shown in Fig. 6. Note that the selected algorithm effectively eliminates the particles adjacent to the boundaries of the camera FOV, which do not form any physical surface. It is seen that beginning with scan #7, the surface of selected domain (blue-colored in Fig. 4) becomes visible and that this domain grows until it is confined by the boundaries of neighboring domains and by the near-electrode sheath. A little difference between the fronts for scans #10 and 11 is indicative of the fact that the domain growth stops at this time. Obviously, the whole crystallization front has no definite shape. Since the front velocity is correctly determined only for a plane front propagating along a certain direction, we have to search for such a plane area of the front and for the corresponding direction of propagation.

IV. MEASUREMENT OF THE FRONT VELOCITY

Measurement of the 3D crystallization front propagation velocity encounters two principal problems. First, the time between successive scans is long enough so that the path of a small front area can be curvilinear and therefore, it cannot be measured. This makes even a physical definition of the front velocity problematic. Second, the front velocity v cannot be fully neglected as

compared with the scan velocity u . Hence, the visible domain surface determined in the depth scan is different from the real one. Both difficulties are obviated if we assume that there exists a small area of the domain surface that can be approximated by a plane and that propagates along a certain line with the normal to this area $\mathbf{n} = \{n_x; n_y; n_z\}$ parallel to this line (\mathbf{n} is directed like the propagation velocity). We will term such small area the reference area and define the front propagation velocity v as the velocity of the reference area motion along \mathbf{n} .

Consider a pair of even or odd scans, for which the visible reference areas are parallel. The normal to the visible reference area \mathbf{n}' can be related to \mathbf{n} . Consider a pair of the odd scans, 1 and 2, when the dust cloud is scanned in the direction of the Y -axis. Then the plane of the laser sheet during scan 1 is defined by the equation $y = u(t - \tau_1)$, where t is the time and τ_1 designates the start time of scan 1. The equation for the “true” reference area is $\mathbf{n} \cdot \mathbf{r} = vt$, where \mathbf{r} designates space coordinates. The visible reference area is a plane, in which the intersection between the laser sheet plane and the “true” reference area moves. We exclude the time from the equations defining the laser sheet plane and the reference area to obtain

$$\mathbf{n}' \cdot \mathbf{r} = r_1 = \frac{v\tau_1}{\eta}, \quad \mathbf{n}' = \left\{ \frac{n_x}{\eta}; \frac{n_y - \beta}{\eta}; \frac{n_z}{\eta} \right\}, \quad (5)$$

where r_1 is the distance between the visible reference area and the origin of the coordinate system,

$$\eta = \sqrt{n_x^2 + (n_y - \beta)^2 + n_z^2} \simeq 1 - \beta n_y \simeq 1 - \beta n'_y \quad (6)$$

and $\beta = v/u$, which is assumed to be small, $\beta \ll 1$.

We approximate the visible reference area by a secant plane that is close to the tangential plane perpendicular to the normal \mathbf{n}' . We find a small group of m particles in the vicinity of the point of intersection between the front propagation line and the domain surface with the radius-vectors \mathbf{r}_i that maximize the dot product $\mathbf{r}_i \cdot \mathbf{n}'$. The radius-vector of the center of mass of the selected group is

$$\mathbf{R}_c^{(1)} = \frac{1}{m} \sum_{i=1}^m \mathbf{r}_i \quad (7)$$

and its projection on the direction of \mathbf{n}' is

$$r_1 = \mathbf{n}' \cdot \mathbf{R}_c^{(1)} = \frac{1}{m} \sum_{i=1}^m \mathbf{r}_i \cdot \mathbf{n}'. \quad (8)$$

It follows from Eqs. (5) and (6) that

$$\beta u \tau_1 = (\beta n'_y - 1) r_1. \quad (9)$$

For the next odd scan, $\beta u \tau_2 = (\beta n'_y - 1) r_2$, where τ_2 is the start time of scan 2 and r_2 is defined by the r.h.s. of

Eq. (8) for scan 2. We subtract (9) from this equation to derive the front velocity between the successive odd scans,

$$v = v_{\text{odd}} = \frac{v_0}{1 + n'_y \frac{v_0}{u}}, \quad v_0 = \frac{r_2 - r_1}{\tau_2 - \tau_1}. \quad (10)$$

As is seen from (10), the front velocity is invariant to the coordinate system and depends solely on the difference of the start times of like scans. The equation for the front velocity between successive even scans differs from (10) by the opposite sign of u ,

$$v = v_{\text{ev}} = \frac{v_0}{1 - n'_y \frac{v_0}{u}}. \quad (11)$$

The last term in the denominator of (10) and (11) is the correction for a finite scan velocity.

Since the rectilinear propagation of the reference area perpendicular to the line of propagation can be characterized by the coincidence of directions of the vector $\mathbf{R}_c^{(2)} - \mathbf{R}_c^{(1)}$ that defines the propagation line and the “true” normal

$$\mathbf{n} = \{(1 - \beta n'_y)n'_x; (1 - \beta n'_y)n'_y + \beta; (1 - \beta n'_y)n'_z\}, \quad (12)$$

we have to minimize the difference between $\mathbf{R}_c^{(2)} - \mathbf{R}_c^{(1)}$ and its projection on \mathbf{n} ,

$$\rho_c = \left| \mathbf{n} \times \left(\mathbf{R}_c^{(2)} - \mathbf{R}_c^{(1)} \right) \right|, \quad (13)$$

by variation of \mathbf{n}' . Here, we ignore unphysical boundary value maxima corresponding to the propagation directions that are almost parallel to the boundaries of the camera FOV. At the same time, we check that the reference area is not a part of the interface between two domains.

Thus, the front propagation velocity is determined as follows. For every treated domain, we resolve its visible surface at each scan, then we select relevant pairs of the consecutive odd-odd or even-even scans. For a pair of scans, we adjust \mathbf{n}' to minimize ρ_c (13) using formulas (7) and (12). In this way, we determine both the propagation direction and velocity (Eqs. (8), (10), and (11)).

Figure 7 illustrates the results of minimization procedure for the pair of scans #8 and 10. It is seen that the difference between \mathbf{n}' and \mathbf{n} (propagation direction) is noticeable, so that the correction for the finite scan velocity is appreciable. We have found that the optimum number of particles comprising the reference area is $m = 50$ and the resulting $\rho_c = 23 \mu\text{m}$ while the interparticle distance is $n_d^{-1/3} = 111 \mu\text{m}$. The condition $\rho_c n_d^{1/3} \ll 1$ satisfied for our system is indicative of the fact that there exists at least one rectilinear propagation direction and corresponding reference area.

We applied the above-discussed procedure for the two largest domains, namely, the blue-colored and magenta-colored ones in Fig. 4. Other domains have too small

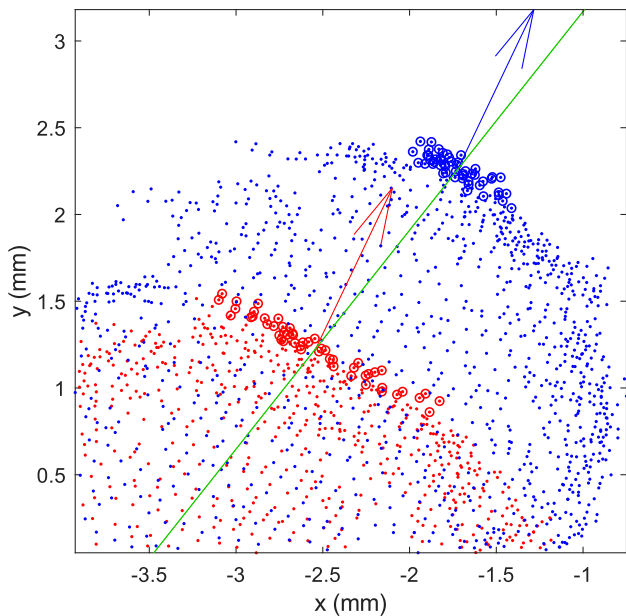


FIG. 7. Illustration of the rectilinear propagation front velocity measurement for scans #8 and 10 (blue-colored domain in Fig. 4). Red dots indicate the domain surface for scan #8 and blue dots, for scan #10; circled dots show the particles that comprise the reference areas. Green line indicates the propagation direction parallel to the “true” normal \mathbf{n} ; red and blue arrows show the vector \mathbf{n}' starting at the centers of mass of the reference areas for corresponding scans.

surface at the scans #7–10 to be processed. For the blue-colored domain, the pair of scans #8 and 10 is a single one that satisfies our conditions. Indeed, for the odd pair #7 and 9, the propagation line passes outside the domain surface at scan #7, which is partly invisible (Fig. 6). For the same reason, we failed to find a non-boundary minimum of ρ_c for this scan pair. In the last pair of scans (#9 and 11), the reference area for scan #11 is a boundary between two neighboring domains (Fig. 4). For this reason, this pair is unusable. However, given the propagation line determined for scans #8 and 10 (black line in Fig. 6), one can calculate the distance between its intersections with the domain surfaces (the front displacement) for all possible scan pairs as $\Delta S = \mathbf{n} \cdot (\mathbf{r}_2 - \mathbf{r}_1)$, where \mathbf{r}_2 and \mathbf{r}_1 are the radius-vectors of the particles pertaining to the surface of corresponding domain that are situated at the closest distance from the propagation line. The coordinates z of such particles are unambiguously related to the instants τ_2 and τ_1 , at which they are illuminated by the laser sheet. Note that there is no real point of intersection between the propagation line and the scan #7 surface. The corresponding time difference $\Delta\tau = \tau_2 - \tau_1$ enables determination of the front velocity by such point measurement, $v = \Delta S / \Delta\tau$. For the magenta-colored domain in Fig. 4, the point measurement is redundant because all three pairs of scans, #7 and 9, #8 and 10, and #9 and 11 can be processed.

We performed similar experiment for the argon pres-

sure of 15 Pa. In this case, we also found the two largest domains with sufficient area of the solid–liquid interface (domains #3 and 4). The rectilinear propagation way of the velocity measurement is applicable to the pairs of scans #9–11, #10–12, #11–13, and #12–14 (domain #3) and #11–13 and #12–14 (domain #4).

V. RESULTS AND DISCUSSION

The minimization procedure discussed in Sec. IV yields the estimation for the front velocity $v \simeq 59 \mu\text{m s}^{-1}$. The results of measurements performed for four domains are summarized in Fig. 8. This figure is indicative of the fact that the velocity of crystallization front is almost independent both of the propagation time and of the spatial position in the dust cloud. Note that a sharp drop of the velocity after 40 s is accounted for by the contact between the boundaries of neighboring domains. This contact can increase the tension inside the domains and thus shift them toward the crystallization–melting binodal. A good agreement between the velocities determined by the minimization procedure for all domains and the point measurement is worth mentioning (Fig. 8). The results for the argon pressure of 15 Pa are not much different from that for 10 Pa. It is seen in Fig. 8 that the front velocity is somewhat higher than that for 10 Pa and reveals a low maximum followed by the velocity fall. However for both pressures, most of the data are grouped in the interval from 60 to 80 $\mu\text{m s}^{-1}$. Note that for 15 Pa, as domains become visible in the camera FOV, they contact each other so that the surface area of the domain–domain interface is substantial. Extensive contacts between the domains can modify the front velocity but the surface area of such contacts can hardly be measured in experiments. In contrast, the measurements using the domains #1 and 2 correspond to the growth of free domains, which increases the reliability of these data. Since for different domains, the front propagation directions are different, one can conclude that the front propagation velocity is independent of the direction, in which it is measured.

Apparently, the Coulomb coupling parameter is the most important one that can affect the front velocity. For the treated dust cloud, we estimate it using the results of our previous study [30],

$$\Gamma = \frac{Z^2 e^2}{r_d k_B T_d} = 3 \left(\frac{r_d}{\delta r} \right)^2, \quad (14)$$

where Z is the dust particle charge in units of the electron charge, e is the elementary electric charge, k_B is the Boltzmann constant, $T_d = 2K/3k_B$, and K are the kinetic temperature and energy of the particles, respectively, $r_d = (3/4\pi n_d)^{1/3}$ is the Wigner–Seitz radius for a dust particle, and δr is the 3D standard deviation of a particle from its equilibrium position in this cell. The Coulomb coupling parameter measured for the runs without the depth scans proves to be almost constant in the region of front propagation and amounts to 54 for 10 Pa

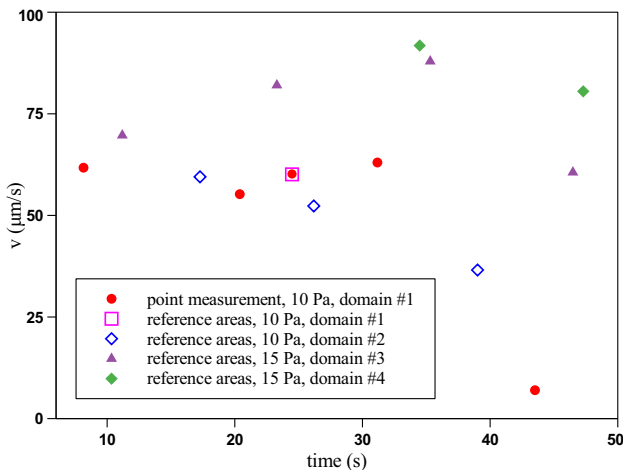


FIG. 8. Crystallization front propagation velocity determined from the rectilinear propagation velocity definition for the domain #1 (open square), #2 (open diamonds), #3 (triangles), and #4 (solid diamonds), and by the dot measurement for the domain #1 (circles). The domains #1 and 2 correspond to the experiment with the argon pressure of 10 Pa, the domains #3 and 4, to 15 Pa. The time is counted from the start of a scan for which the domains #1 and 3 are first visible in the camera FOV for the gas pressure of 10 and 15 Pa, respectively.

and to 49 for 15 Pa. Such a low value seems to be meaningful because for $2.55 \mu\text{m}$ diameter particles, $\Gamma \sim 150$ and it drops with the decrease of the particle diameter [30]. Thus, we can conclude that we have measured the 3D velocity of the crystallization front propagating in complex plasma. This result is compatible with that of study [17], where the estimated vertical 2D velocity of the crystallization front was about one interparticle distance per second.

VI. CONCLUSION

In this study, we have investigated the kinetics of the first-order phase transition in complex plasma, namely, the propagation of the crystallization front through the cloud of charged dust particles under microgravity conditions. Based on PK-3 Plus laboratory onboard the ISS, we used the function generator to prepare a “supercooled” state of the liquidlike dust cloud in plasma of a low-pressure argon discharge. We observed growth of the crystal domains in the dust cloud. The data obtained from the depth scans of this particle subsystem enabled us to obtain the 3D particle coordinates. Then we tried two approaches that can divide all particles into “liquidlike” and “solidlike” ones. The correlation criterion related to the rotational invariants can effectively distinguish between the particle types. However, it cannot separate different crystal domains and their surfaces. For this reason, we put forward the determination of the principal axes directions for each crystal that comprises a domain. This enables us not only to identify the “solid-

like” particles but to separate effectively different domains. Comparison between these approaches shows that they identify almost the same particles as the “solidlike” ones. The method of the domain surface determination we used allows one to isolate a set of the pivot particles that represent directly the propagating front.

A key point in the front velocity measurement is determination of the propagation line direction. This implies that there exists a small area of the domain surface propagating along this line perpendicularly to it that we term the reference area. We find such line by minimization of the projection of the vector connecting the reference area centers of the corresponding unidirectional scans on the normal to these areas. Here, we take into account rotation of the visible normals due to the finite scan velocity. In the course of this procedure, the crystallization front velocity is calculated. This is a true 3D front velocity that is an important property of the plasma crystallization kinetics. Alternatively, one can calculate the velocity dividing the distances between the points of intersection between the propagation line and the domain surfaces by the corresponding time intervals.

Eventually, we have found that the front velocity is almost constant for our system and it amounts to ca. $60\text{--}80 \mu\text{m s}^{-1}$, which is less than the interparticle distance per second. A good agreement between the point measurement and the rectilinear propagation velocity definition is noteworthy. We have shown that the front propagates in a uniform dust cloud and it is decelerated when the surfaces of neighboring domains are brought in contact.

2D measurements show solely the line of the boundary of the domain cross-section by the laser sheet plane. As the domain grows, different points of its surface intersect with the laser sheet. We suppose that it is impossible to find a physical definition of the front velocity based on the 2D measurements. Instead, the proposed 3D definition of this quantity along the direction of the rectilinear propagation is definite and it is a relevant characteristic of the corresponding physical process.

The problems to be addressed in future are development of a theory of the plasma crystal growth and treatment of very small crystal clusters in the liquid (crystal-lites), which were neglected in this study. Investigations in these trends can contribute to development of the theory of strongly coupled plasma crystallization.

ACKNOWLEDGMENTS

The PK-3 Plus laboratory project was supported by ROSCOSMOS. This project was also funded by Deutsches Zentrum für Luft- und Raumfahrt e.V. with funds from the Federal Ministry for Economy and Technology according to a resolution of the Deutscher Bundestag under grant numbers 50WM0203 and 50WM1203.

REFERENCES

-
- [1] V. E. Fortov and G. E. Morfill, eds., *Complex and Dusty Plasmas: From Laboratory to Space*, Series in Plasma Physics (CRC Press, Boca Raton, FL, 2010).
- [2] J. H. Chu and Lin I, *Phys. Rev. Lett.* **72**, 4009 (1994).
- [3] H. Thomas, G. E. Morfill, V. Demmel, J. Goree, B. Feuerbacher, and D. Möhlmann, *Phys. Rev. Lett.* **73**, 652 (1994).
- [4] S. V. Vladimirov, K. Ostrikov, and A. A. Samarian, *Physics and Applications of Complex Plasmas* (Imperial College, London, 2005).
- [5] V. Fortov, A. Ivlev, S. Khrapak, A. Khrapak, and G. Morfill, *Phys. Rep.* **421**, 1 (2005).
- [6] M. Bonitz, C. Henning, and D. Block, *Rep. Prog. Phys.* **73**, 066501 (2010).
- [7] C. K. Goertz, *Rev. Geophys.* **27**, 271 (1989).
- [8] G. E. Morfill, U. Konopka, M. Kretschmer, M. Rubin-Zuzic, H. M. Thomas, S. K. Zhdanov, and V. Tsytovich, *New J. Phys.* **8**, 7 (2006).
- [9] M. Schwabe, S. K. Zhdanov, H. M. Thomas, A. V. Ivlev, M. Rubin-Zuzic, G. E. Morfill, V. I. Molotkov, A. M. Lipaev, V. E. Fortov, and T. Reiter, *New J. Phys.* **10**, 033037 (2008).
- [10] G. E. Morfill, H. M. Thomas, U. Konopka, H. Rothermel, M. Zuzic, A. Ivlev, and J. Goree, *Phys. Rev. Lett.* **83**, 1598 (1999).
- [11] S. A. Khrapak, B. A. Klumov, P. Huber, V. I. Molotkov, A. M. Lipaev, V. N. Naumkin, H. M. Thomas, A. V. Ivlev, G. E. Morfill, O. F. Petrov, V. E. Fortov, Yu. Malentschenko, and S. Volkov, *Phys. Rev. Lett.* **106**, 205001 (2011).
- [12] H. M. Thomas, G. E. Morfill, V. E. Fortov, A. V. Ivlev, V. I. Molotkov, A. M. Lipaev, T. Hagl, H. Rothermel, S. A. Khrapak, R. K. Suetterlin, M. Rubin-Zuzic, O. F. Petrov, V. I. Tokarev, and S. K. Krikalev, *New J. Phys.* **10**, 033036 (2008).
- [13] K. Jiang, V. Nosenko, Y. F. Li, M. Schwabe, U. Konopka, A. V. Ivlev, V. E. Fortov, V. I. Molotkov, A. M. Lipaev, O. F. Petrov, M. V. Turin, H. M. Thomas, and G. E. Morfill, *Europhys. Lett.* **85**, 45002 (2009).
- [14] M. Schwabe, K. Jiang, S. Zhdanov, T. Hagl, P. Huber, A. V. Ivlev, A. M. Lipaev, V. I. Molotkov, V. N. Naumkin, K. R. Sütterlin, H. M. Thomas, V. E. Fortov, G. E. Morfill, A. Skvortsov, and S. Volkov, *Europhys. Lett.* **96**, 55001 (2011).
- [15] V. N. Naumkin, A. M. Lipaev, V. I. Molotkov, D. I. Zhukhovitskii, A. D. Usachev, and H. M. Thomas, *J. Phys.: Conf. Series* **946**, 012144 (2018).
- [16] G. Chabrier and E. Schatzman, eds., *The Equation of State in Astrophysics* (Cambridge University Press, Cambridge, UK, 1994).
- [17] M. Rubin-Zuzic, G. E. Morfill, A. V. Ivlev, R. Pompl, B. A. Klumov, W. Bunk, H. M. Thomas, H. Rothermel, O. Havnes, and A. Fouqué, *Nature Phys.* **2**, 181 (2006).
- [18] U. Gasser, E. R. Weeks, A. Schofield, P. N. Pusey, and D. A. Weitz, *Science* **292**, 258 (2001).
- [19] U. Gasser, *J. Phys.: Condens. Matter* **21**, 203101 (2009).
- [20] A. G. Khrapak, V. I. Molotkov, A. M. Lipaev, D. I. Zhukhovitskii, V. N. Naumkin, V. E. Fortov, O. F. Petrov, H. M. Thomas, S. A. Khrapak, P. Huber, A. Ivlev, and G. Morfill, *Contrib. Plasma Phys.* **56**, 253 (2016).
- [21] V. N. Naumkin, D. I. Zhukhovitskii, V. I. Molotkov, A. M. Lipaev, V. E. Fortov, H. M. Thomas, P. Huber, and G. E. Morfill, *Phys. Rev. E* **94**, 033204 (2016).
- [22] H. M. Thomas, M. Schwabe, M. Y. Pustylnik, C. A. Knapek, V. I. Molotkov, A. M. Lipaev, O. F. Petrov, V. E. Fortov, and S. A. Khrapak, *Plasma Physics and Controlled Fusion* **61**, 014004 (2019).
- [23] M. Schwabe, C.-R. Du, P. Huber, A. M. Lipaev, V. I. Molotkov, V. N. Naumkin, S. K. Zhdanov, D. I. Zhukhovitskii, V. E. Fortov, and H. M. Thomas, *Microgravity Science and Technology* **30**, 581 (2018).
- [24] A. V. Ivlev, G. E. Morfill, H. M. Thomas, C. R ath, G. Joyce, P. Huber, R. Kompaneets, V. E. Fortov, A. M. Lipaev, V. I. Molotkov, T. Reiter, M. Turin, and P. Vinogradov, *Phys. Rev. Lett.* **100**, 095003 (2008).
- [25] P. J. Steinhardt, D. R. Nelson, and M. Ronchetti, *Phys. Rev. B* **28**, 784 (1983).
- [26] P. R. ten Wolde, M. J. RuizMontero, and D. Frenkel, *J. Chem. Phys.* **104**, 9932 (1996).
- [27] B. A. Klumov, Y. Jin, and H. A. Makse, *The Journal of Physical Chemistry B* **118**, 10761 (2014).
- [28] J. A. van Meel, L. Filion, C. Valeriani, and D. Frenkel, *J. Chem. Phys.* **136**, 234107 (2012).
- [29] A. K. Jain, *Pattern Recognition Letters* **31**, 651 (2010), 19th International Conference on Pattern Recognition (ICPR 2008), Tampa, FL, DEC 08-11, 2008.
- [30] D. I. Zhukhovitskii, V. N. Naumkin, A. I. Khusnulgatin, V. I. Molotkov, and A. M. Lipaev, *Phys. Rev. E* **96**, 043204 (2017).
- [31] C. Dietz, R. Bergert, B. Steinm uller, M. Kretschmer, S. Mitic, and M. H. Thoma, *Phys. Rev. E* **97**, 043203 (2018).
- [32] D. I. Zhukhovitskii, *J. Chem. Phys.* **125**, 234701 (2006).